

1      **Impact of grids and dynamical cores in CESM2.2 on**  
2      **the meteorology and climate of the Arctic**

3      **Adam R. Herrington** <sup>1</sup>, **Marcus Lofverstrom** <sup>2</sup>, **Peter H. Lauritzen** <sup>1</sup> and  
4      **Andrew Gettelman** <sup>1</sup>

5      <sup>1</sup>National Center for Atmospheric Research, 1850 Table Mesa Drive, Boulder, Colorado, USA  
6      <sup>2</sup>Department of Geosciences, University of Arizona, 1040 E. 4th Street, Tucson, AZ USA

7      **Key Points:**

- 8      • enter point 1 here  
9      • enter point 2 here  
10     • enter point 3 here

**Abstract**

[ enter your Abstract here ]

**Plain Language Summary**

[ enter your Plain Language Summary here or delete this section]

**1 Introduction**

General Circulation Models (GCMs) are powerful tools for understanding the meteorology and climate of the high-latitudes, which are among the most sensitive regions on Earth to global and environmental change. Despite their importance, the numerical treatment of polar regions in GCMs is handled in vastly-different ways due to the so-called *pole-problem* (D. Williamson, 2007), which refers to numerical instability arising from the convergence of meridians at the polar points on latitude-longitude grids (e.g., Figure 1a). Depending on the numerics, methods exist to suppress this instability, and latitude-longitude grids may be advantageous for polar processes as structures can be represented with more degrees of freedom than elsewhere in the computational domain. With the recent trend towards globally uniform unstructured grids, any potential benefits of latitude-longitude grids on polar regions may become a relic of the past. In this study, a spectrum of model grids and dynamical cores (hereafter referred to as *dycores*) available in the Community Earth System Model, version 2.2 (CESM; <http://www.cesm.ucar.edu/models/cesm2/>) are evaluated to understand their impacts on the simulated characteristics of the Arctic, with a special focus on the meteorology over the Greenland Ice Sheet.

In the 1970's the pole problem was largely defeated through wide-spread adoption of efficient spectral transform methods in GCMs. These methods transform grid point fields into a global, isotropic representation in wave space, where linear operators (e.g. horizontal derivatives) in the equation set can be solved for exactly. While spectral transform methods are still used in the 21st century, local numerical methods have become desirable for their ability to run efficiently on massively parallel systems. The pole-problem has thus re-emerged in contemporary climate models that use latitude-longitude grids, and some combination of reduced grids and polar filters are necessary to ameliorate this instability (Jablonowski & Williamson, 2011). Polar filters are akin to a band-aid; they subdue the growth of unstable modes by applying additional damping to the solution over polar regions. One might expect that this additional damping reduces the effective resolution such that the resolved scales are similar across the entire domain, but this seems unlikely (describe why) and is explored further in this study.

An alternative approach is to use unstructured grids, which allow for more flexible grid structures that permit quasi-uniform grid spacing globally and eliminates the pole-problem entirely (e.g., Figure 1c). This grid flexibility also allows for variable-resolution or regional grid refinement (e.g., Figure 2). Grids can be developed with refinement over polar regions that could in principle make up for any loss in polar resolution in transitioning away from latitude-longitude grids (e.g., Figure 2), although this comes at the cost of a smaller CFL-limiting time-step in the refined region (the CFL-condition — short for Courant–Friedrichs–Lowy condition — is a necessary condition for numerical stability when using discrete data in time and space). However, unstructured grids scale more efficiently on parallel systems than latitude-longitude grids, likely resulting in a greater prevalence of unstructured grids as computing power continued to increase over time.

The meteorology and climate of the Arctic is characterized by a range of processes and scales that are difficult to represent in GCMs (Bromwich et al., 2001; Smirnova & Golubkin, 2017; van Kampenhout et al., 2018). For example, while synoptic scale storms

are generally well represented at typical GCM resolutions of 1 to 2 degrees (Jablonowski & Williamson, 2006; Stocker, 2014), mesoscale Polar Lows are not well resolved at these resolutions. These mesoscale systems are prevalent during the cold season and produce gale-force winds that can induce large heat and moisture fluxes through the underlying sea-ice/ocean interface. The Arctic also contains the Greenland Ice Sheet (hereafter denoted as *GrIS*). While it blankets the largest island in the world (Greenland), many of the processes that control the *GrIS* annual surface mass balance (the integrated sum of precipitation and melting) are only partially resolved at typical GCM resolutions. For example, *GrIS* precipitation is typically confined to the ice-sheet margins (predominately the southeastern margin) where orographic precipitation is generated by steep topographic slopes. Moreover, *GrIS* ablation areas (marginal regions where seasonal melting exceeds the annual mass input from precipitation) are typically 10s to 100 km wide and confined to low-level areas or regions with limited precipitation. GCMs struggle to resolve the magnitude and extent of these features (van Kampenhout et al., 2018), which can lead to unrealistic ice sheet growth in models with an interactive ice sheet component (e.g., Lofverstrom et al., 2020).

The goal of this study is to characterize the representation of high-latitude regions using the spectral-element and finite-volume dycores in CESM2.2, as these models treat the high-latitudes, e.g., the pole-problem, in different ways. The manuscript is laid out as follows: Section 2 consists of documentation of the grids, dycores and physical parameterizations used in this study. The Arctic refined grids were developed by the authors, and this section serves as their official documentation in CESM2.2. Section 2 also contains a description of the experiments along with reanalysis datasets and post-processing software used for evaluating the model simulations. Section 3 contains the results of the experiments, followed by Section 4 that provides a general discussion and conclusions.

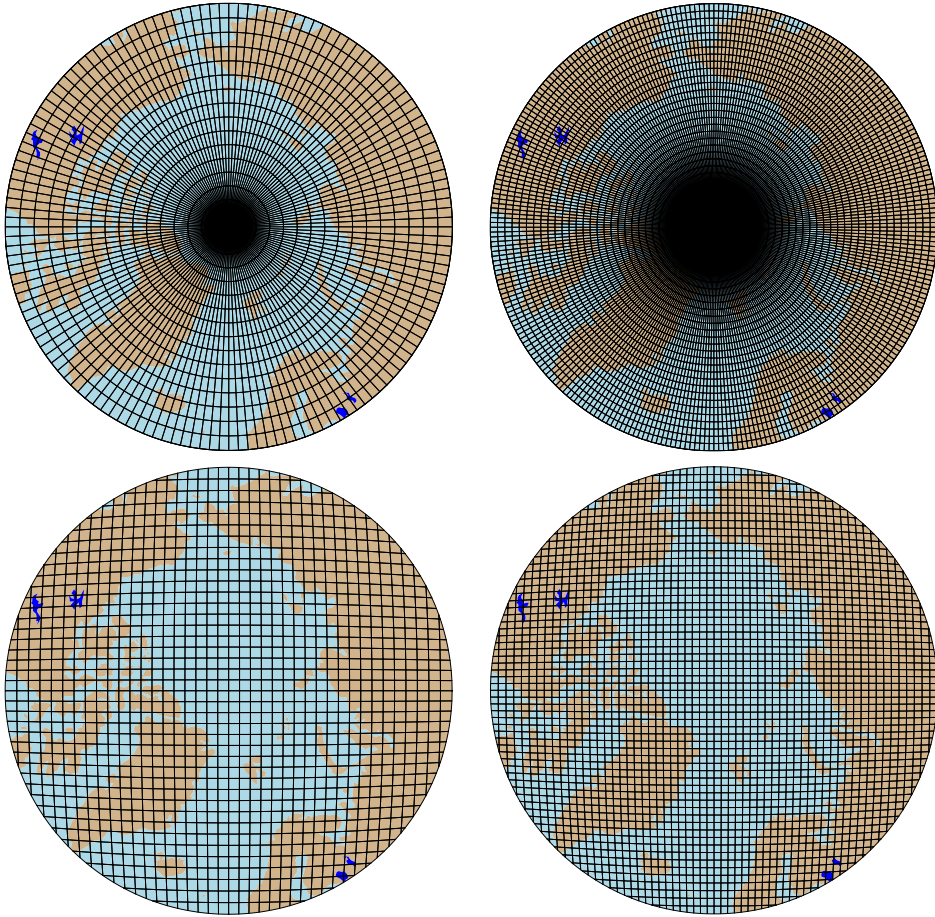
## 2 Methods

### 2.1 Dynamical cores

The atmospheric component of CESM2.2, the Community Atmosphere Model, version 6.3 (CAM; <https://ncar.github.io/CAM/doc/build/html/index.html>), supports a number of different atmospheric dynamical cores. These include dycores using latitude-longitude grids, such as finite-volume (FV; Lin, 2004) and eulerian spectral transform (EUL; Collins et al., 2006) models, and dycores built on unstructured grids, including spectral-element (SE; Lauritzen et al., 2018) and finite-volume 3 (FV3; Putman & Lin, 2007) models. The EUL dycore is the oldest dycore in CAM, and the least supported of all the dycores in the current model. FV3 is the newest dycore in CAM, but it was not fully incorporated at the time this work commenced; both the EUL and FV3 dycores are omitted from this study. As such, the results presented in this study are comparing the performance of the SE and FV dycores.

#### 2.1.1 Finite-volume (FV) dynamical core

The FV dycore is a hydrostatic model that integrates the equations of motion using a finite-volume discretization on a spherical latitude-longitude grid (Lin & Rood, 1997). The 2D dynamics evolve in floating Lagrangian layers that are periodically mapped to Eulerian reference grid in the vertical (Lin, 2004), using a hybrid-pressure vertical coordinate. Hyperviscous damping is applied to the divergent modes while Laplacian damping is applied to momentum in the top few layers, referred to as a *sponge layer* (Lauritzen et al., 2011). A polar filter is used to avoid computational instability due to the convergence of the meridians, allowing for a more practical time-step. It takes the form of a Fourier filter in the zonal direction, with the damping coefficients increasing monotonically in the poleward direction (Suarez & Takacs, 1995).

**Figure 1.** .

### 108      *2.1.2 Spectral-element (SE) dynamical core*

109      The SE dycore is a hydrostatic model that integrates the equations of motion us-  
 110      ing a high-order continuous Galerkin method (Taylor et al., 1997; Dennis et al., 2012).  
 111      The computational domain is a cubed-sphere grid tiled with quadrilateral elements (e.g.,  
 112      Figure 2). Each element contains a fourth order basis set in each horizontal direction,  
 113      with the solution defined at the roots of the basis functions, the Gauss-Lobatto-Legendre  
 114      (GLL) quadrature points. This results in 16 GLL nodal points within each element, with  
 115      12 of the points lying on the (shared) element boundary. Communication between el-  
 116      ements happens via the direct stiffness summation (Canuto et al., 2007), which applies  
 117      a numerical flux to the element boundaries that reconciles overlapping nodal values and  
 118      produces a continuous global basis set.

119      As with the FV dycore, the dynamics evolve in floating Lagrangian layers that are  
 120      subsequently mapped to an Eulerian reference grid. A dry mass vertical coordinate was  
 121      more recently implemented for thermodynamic consistency with condensates (Lauritzen  
 122      et al., 2018). The 2D dynamics have no implicit dissipation and so hyperviscosity op-  
 123      erators are applied to all prognostic variables to remove spurious numerical errors (Dennis  
 124      et al., 2012). Laplacian damping is applied in the sponge layer.

125      The SE dycore supports regional grid refinement via its variable-resolution config-  
 126      uration, requiring two enhancements over uniform resolution grids. (1) As the numer-

**Figure 2.**

ical viscosity increases with resolution, explicit hyperviscosity relaxes according to the local element size, reducing in strength by about an order of magnitude per halving of the grid spacing. A tensor-hyperviscosity formulation is used (Guba et al., 2014), which adjusts the coefficients in two orthogonal directions to more accurately target highly distorted quadrilateral elements. (2) The topography boundary conditions need to be smoothed in a way that does not excite grid scale modes, and so the NCAR topography software (Lauritzen et al., 2015) was modified to scale the smoothing radius by the local element size.

For spectral-element grids with quasi-uniform grid spacing, a variant in which tracer advection is computed using the Conservative Semi-Lagrangian Multi-tracer transport scheme (CSLAM) is used instead (Lauritzen et al., 2017). CSLAM has improved tracer property preservation and accelerated multi-tracer transport. It uses a separate grid from the spectral-element dynamics, through dividing each element into  $3 \times 3$  control volumes with quasi-equal area. The physical parameterizations are computed from the state on the CSLAM grid, which has clear advantages over the default SE dycore in which the physics are evaluated at the GLL nodal points (A. Herrington et al., 2018).

## 2.2 Grids

Six grid are evaluated in this study (Table X). The FV dycore is run with  $1^\circ$  and  $2^\circ$  grid spacing, referred to as *f09* and *f19*, respectively (Figure 1a,b). The  $1^\circ$  equivalent of the CAM-SE-CSLAM grid is also run, referred to as *ne30pg3* (Figure 1c), where *ne* refers to a grid with of  $ne \times ne$  elements per cubed-sphere face, and *pg* denotes that there are  $pg \times pg$  control volumes per element for computing the physics. An additional  $1^\circ$  CAM-SE-CSLAM grid is run, but with the physical parameterizations computed on a grid that contains  $2 \times 2$  control volumes per element, *ne30pg2* (Figure 1d; A. R. Herrington et al., 2019).

Two variable resolution meshes were developed as part of the CESM2.2 release that contains grid refinement over the Arctic (Figure 2). The Arctic meshes were developed using the software package SQuadgen (<https://github.com/ClimateGlobalChange/squadgen>). The *ARCTIC* grid is a  $1^\circ$  grid with  $\frac{1}{4}^\circ$  regional refinement over the broader Arctic region. The *ARCTICGRIS* grid is identical to the *ARCTIC* grid, but contains an additional patch covering the big island of Greenland with  $\frac{1}{8}^\circ$  resolution.

### 158      2.3 Physical parameterizations

159      The CAM6 physical parameterization package (hereafter referred to as the *physics*;  
 160      <https://ncar.github.io/CAM/doc/build/html/index.html>) is used for all simula-  
 161      tions in this study. CAM6 physics is most noteably different from it's predecessors through  
 162      the incorporation of high-order turbulence closure, Cloud Layers Unified by Binormals  
 163      (CLUBB; Golaz et al., 2002; Bogenschutz et al., 2013), which jointly acts as a PBL, shal-  
 164      low convection and cloud macrophysics scheme. CLUBB is coupled with the MG2 mi-  
 165      crophysics scheme (Gettelman et al., 2015), with prognostic precipitation and classical  
 166      nucleation theory in representing cloud ice for improved cloud-aerosol interactions. Deep  
 167      convection is parameterized using a convective quasi-equilibrium mass flux scheme (Zhang  
 168      & McFarlane, 1995; Neale et al., 2008) inclusing convective momentum transport (Richter  
 169      et al., 2010). PBL form drag is modeled after (Beljaars et al., 2004) and orographic grav-  
 170      ity wave drag is represented with an anisotropic method informed by the orientation of  
 171      topographic ridges at the sub-grid scale.

172      The CAM convention is that the physics package determines the vertical resolu-  
 173      tion. Since all runs use CAM6 physics, all grids and dycores use 32 levels in the verti-  
 174      cal, with a model top of about 1 hPa or about 40 km. The physics time-step, in con-  
 175      trast, is dependent on grid resolution. Increases in horizontal resolution permit faster  
 176      vertical velocities that reduce characteristic time-scales, and so the physics time-step should  
 177      be reduced to avoid large time truncation errors (A. Herrington & Reed, 2018). The *ARCTIC*  
 178      and *ARCTICGRIS* grids are therefore run with a 4× and 8× reduction in physics time-  
 179      step relative to the default 1800 s time-step used in coarser, uniform resolution grids.

### 180      2.4 Experimental design

181      All grids and dycores are run using an identical transient 1979-1998 AMIP-style  
 182      configuration, with prescribed monthly SST/sea-ice after (Hurrell et al., 2008). This con-  
 183      figuration refers to the *FHIST compset* and runs out of the box in CESM2.2. The Com-  
 184      munity Land Model (CLM5; [https://escomp.github.io/ctsm-docs/versions/release](https://escomp.github.io/ctsm-docs/versions/release-clm5.0/html/users_guide/index.html)  
 185      -clm5.0/html/users\_guide/index.html), which uses the same grid as the atmosphere  
 186      grid, calculates the surface energy balance at each land tile within a grid cell, which is  
 187      used to compute snow and bare ice melting to inform the surface mass balance (SMB)  
 188      of a glacier unit (van Kampenhout et al., 2020). For land ice tiles coinciding with the  
 189      Antarctic and Greenland Ice Sheets, the surface energy and mass balance are evaluated  
 190      at ten elevation classes, and integrated over sub-grid hypsometric area-elevation bins for  
 191      more accurate estimation of the surface mass balance of the big ice sheets. Ice accumu-  
 192      lation is modeled as a capping flux, or snow in excess of the assumed 10 m snow cap, and  
 193      refreezing of liquid within the snowpack additionally acts as a source of mass in the SMB  
 194      calculation. Since the 10 m snowcap needs to be reached in the accumulation zone to  
 195      simulate the SMB, the snow depths in the variable-resolution grids were spun-up by forc-  
 196      ing CLM5 offline, cycling over 20 years of a fully coupled *ARCTIC* run for about 500  
 197      years. The uniform resolution grids are all initialized with an SMB from an existing *f09*  
 198      spun-up initial condition.

## 199      3 Results

### 200      3.1 Tropospheric temperatures

201      Before delving into the simulated characteristics of the Arctic, the global mean dif-  
 202      ferences between the grids and dycores are assessed, Figure 3 shows the climatological,  
 203      zonal mean height plots expressed as differences between the uniform resolution grids  
 204      and dycores. The *f09* grid is warmer than the *f19* grid, primarily in the mid-to-high lat-  
 205      itudes and throughout the depth of the troposphere. This is a common response to in-  
 206      creasing horizontal resolution in GCMs (Pope & Stratton, 2002; Roeckner et al., 2006),

and (A. R. Herrington & Reed, 2020) has shown that this occurs in CAM due to greater resolved vertical velocities that in turn, facilitate greater condensational heating in the macrophyics routine in CLUBB. The right columns in Figure 3 supports this interpretation, which shows an increase in the climatological CLUBB heating in the mid-latitudes in the *f09* grid.

As the SE dycore is less diffusive than the FV dycore, the resolved vertical velocities are larger in the SE dycore, and so a modest, resolution-like sensitivity occurs in which *ne30pg3* is warmer than *f09* (Figure 3). The stratosphere has a different response, in which *ne30pg3* is much cooler than *f09* in the mid-to-high latitudes. The differences in temperature between *ne30pg3* and *ne30pg2* are small, with a slight warming near the tropopause at high latitudes. This is consistent with the similar climates found between these grids in (A. R. Herrington et al., 2019).

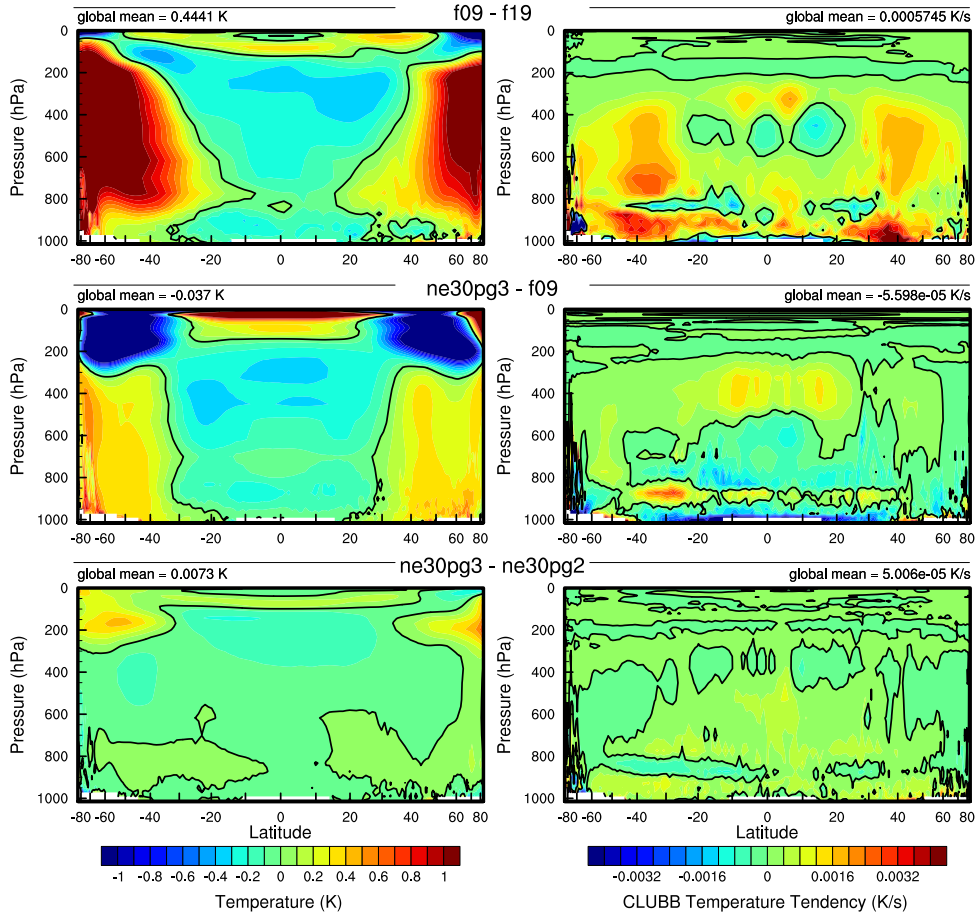
Comparing the variable-resolution grids to the uniform resolution grids is complicated because we are simultaneously increase the grid resolution and reducing the physics time-step, both which noticeably impact the solution (D. L. Williamson, 2008). An additional *ne30pg3* simulations is run with the physics time-step used in the *ARCTIC* grid, referred to as *ne30pg3\**. Figure 4 shows the change in climatological temperature in zonal-mean height space between *ne30pg3\** and *ne30pg3*. A similar warming response to increasing resolution occurs when the time-step is reduced, and the mechanism is similar in that the shorter time-step facilitates greater condensational heating by CLUBB. Figure 4 shows the difference in climatological temperature between the *ARCTIC* grid and the *ne30pg3\** grid. The greater condensational heating and warmer temperatures are confined to the regionally refined region when the impact of physics time-steps is removed from the analysis.

### 3.2 Synoptic-scale storm characteristics

Synoptic storms are identified and analyzed using TempestExtremes (Ullrich et al., 2021). The new *ARCTIC* grid contains  $\frac{1}{4}^{\circ}$  refinement north of about  $45^{\circ}$  latitude, and so the storm tracker is applied to this region for the *ARCTIC* and *ne30pg3* run to identify differences in storm characteristics due to horizontal resolution. Figure 5 shows the mean precipitation rates averaged over all January storms identified by TempestExtremes. The iconic comma structure of the mid-latitude cyclones is simulated in *ne30pg3* and *ARCTIC* grids, with the magnitudes about the same in these two grids, with perhaps a marginal increase in precipitation rates in the storm center of the *ARCTIC* grid. For good measure, the *ne30pg3\** run is also plotted, and looks more-or-less identical to the *ne30pg3* run.

As has been previously reported, horizontal resolution can have large impacts on extreme precipitation events. Figure 6 is a PDF of the precipitation rates associated with synoptic storms, by month. The *ARCTIC* run has larger extreme precipitation rates compared to *ne30pg3* in every month, but the increase is greatest in the summer months, which coincides with the most extreme events of the year. This is primarily due to an increase in resolution; the *ne30pg3\** only marginally increases the precipitation rates compared with *ne30pg3*. It should also be noted that the PDFs are evaluated on an identical composite grid, and so storm statistics are not impacted by differences in dataset resolution.

The extreme precipitation rates in the *ARCTIC* run are closer to the ERA5 reanalysis than in *ne30pg3* (Figure 6). It's difficult to know the extent that the extreme precipitation rates in ERA5 are constrained by data assimilation, or whether these precipitation rates are due to using a similar  $\frac{1}{4}^{\circ}$  model as the *ARCTIC* grid. However, precipitation rates in  $\frac{1}{4}^{\circ}$  models tend to produce more skillful extreme events (O'Brien et al., 2016).

**Figure 3.**

### 257 3.3 Orographic gravity waves emanating from Greenland

### 258 3.4 Katabatic winds emanating from Greenland

### 259 3.5 Greenland surface mass balance

## 260 4 Conclusions

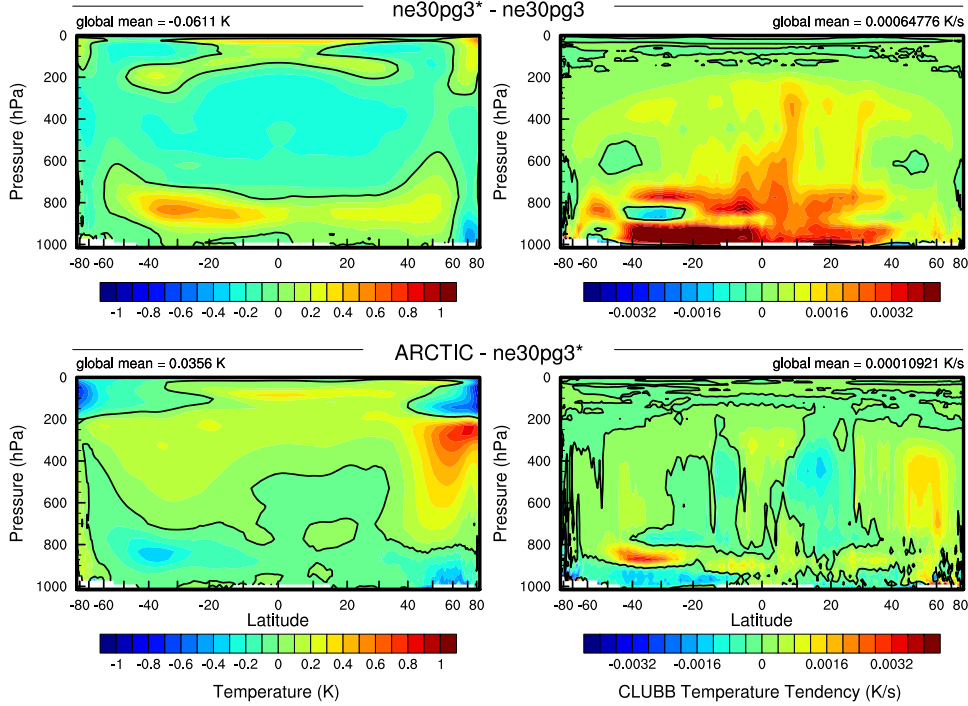
### 261 Acknowledgments

262 This material is based upon work supported by the National Center for Atmospheric Re-  
 263 search (NCAR), which is a major facility sponsored by the NSF under Cooperative Agree-  
 264 ment 1852977. Computing and data storage resources, including the Cheyenne super-  
 265 computer (doi:10.5065/D6RX99HX), were provided by the Computational and Informa-  
 266 tion Systems Laboratory (CISL) at NCAR.

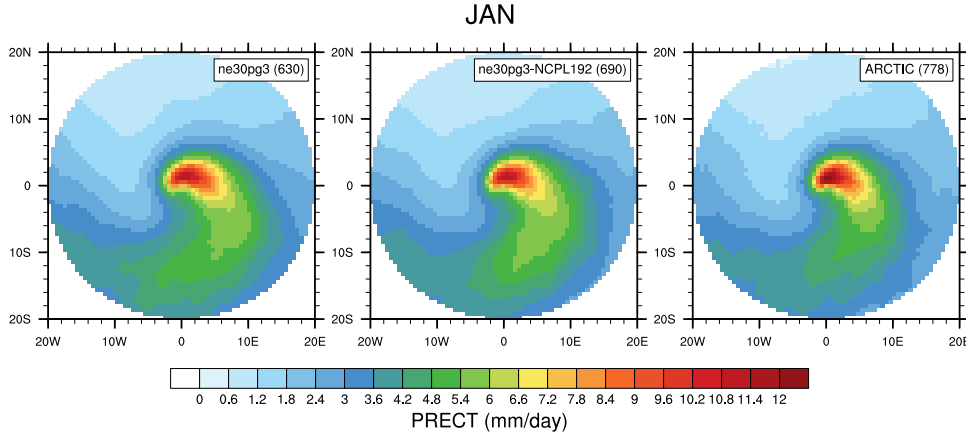
267 The data presented in this manuscript is available at <https://github.com/adamrher/2020-arcticgrids>.

### 269 References

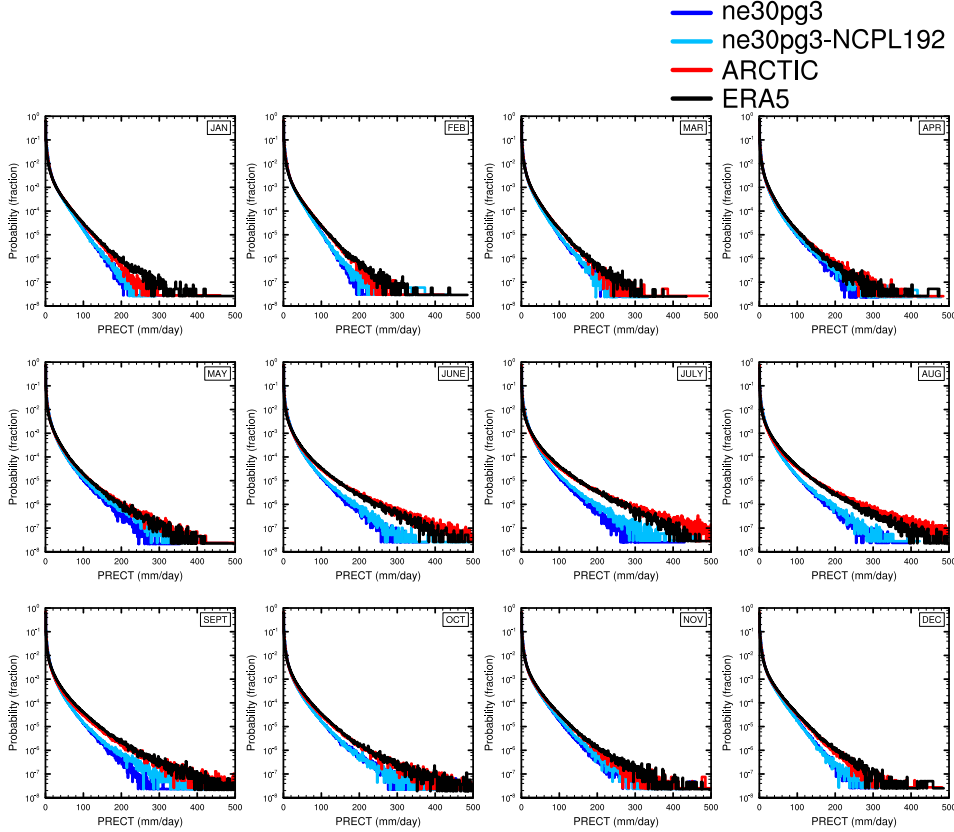
270 Beljaars, A., Brown, A., & Wood, N. (2004). A new parametrization of turbulent

**Figure 4.**

- 271 orographic form drag. *Quart. J. Roy. Meteor. Soc.*, *130*(599), 1327–1347. doi:  
272 10.1256/qj.03.73
- 273 Bogenschutz, P. A., Gettelman, A., Morrison, H., Larson, V. E., Craig, C., & Schaanen,  
274 D. P. (2013). Higher-order turbulence closure and its impact on climate  
275 simulations in the community atmosphere model. *Journal of Climate*, *26*(23),  
276 9655–9676.
- 277 Bromwich, D. H., Cassano, J. J., Klein, T., Heinemann, G., Hines, K. M., Steffen,  
278 K., & Box, J. E. (2001). Mesoscale modeling of katabatic winds over greenland  
279 with the polar mm5. *Monthly Weather Review*, *129*(9), 2290–2309.
- 280 Canuto, C., Hussaini, M. Y., Quarteroni, A., & Zang, T. (2007). *Spectral methods:*  
281 *Evolution to complex geometries and applications to fluid dynamics* (1st ed.).  
282 Springer.
- 283 Collins, W. D., Rasch, P. J., Boville, B. A., Hack, J. J., McCaa, J. R., Williamson,  
284 D. L., ... Zhang, M. (2006). The formulation and atmospheric simulation  
285 of the community atmosphere model version 3 (cam3). *Journal of Climate*,  
286 *19*(11), 2144–2161.
- 287 Dennis, J. M., Edwards, J., Evans, K. J., Guba, O., Lauritzen, P. H., Mirin, A. A.,  
288 ... Worley, P. H. (2012). CAM-SE: A scalable spectral element dynamical  
289 core for the Community Atmosphere Model. *Int. J. High. Perform. C.*, *26*(1),  
290 74–89. Retrieved from <http://hpc.sagepub.com/content/26/1/74.abstract>  
291 doi: 10.1177/1094342011428142
- 292 Gettelman, A., Morrison, H., Santos, S., Bogenschutz, P., & Caldwell, P. (2015).  
293 Advanced two-moment bulk microphysics for global models. part ii: Global  
294 model solutions and aerosol–cloud interactions. *Journal of Climate*, *28*(3),  
295 1288–1307.
- 296 Golaz, J.-C., Larson, V. E., & Cotton, W. R. (2002). A pdf-based model for bound-  
297 ary layer clouds. part i: Method and model description. *Journal of the Atmo-*

**Figure 5.** .

- 298 *spheric Sciences*, 59(24), 3540–3551. doi: 10.1175/1520-0469(2002)059<3540:  
299 apbmfb>2.0.co;2
- 300 Guba, O., Taylor, M. A., Ullrich, P. A., Overfelt, J. R., & Levy, M. N. (2014). The  
301 spectral element method (sem) on variable-resolution grids: evaluating grid  
302 sensitivity and resolution-aware numerical viscosity. *Geosci. Model Dev.*, 7(6),  
303 2803–2816. doi: 10.5194/gmd-7-2803-2014
- 304 Herrington, A., Lauritzen, P., Taylor, M. A., Goldhaber, S., Eaton, B. E., Bacmeis-  
305 ter, J., ... Ullrich, P. (2018). Physics-dynamics coupling with element-based  
306 high-order galerkin methods: quasi equal-area physics grid. *Mon. Wea. Rev.*,  
307 47, 69–84. doi: 10.1175/MWR-D-18-0136.1
- 308 Herrington, A., & Reed, K. (2018). An idealized test of the response of the commu-  
309 nity atmosphere model to near-grid-scale forcing across hydrostatic resolutions.  
310 *J. Adv. Model. Earth Syst.*, 10(2), 560–575.
- 311 Herrington, A. R., Lauritzen, P. H., Reed, K. A., Goldhaber, S., & Eaton, B. E.  
312 (2019). Exploring a lower resolution physics grid in cam-se-cslam. *Journal of*  
313 *Advances in Modeling Earth Systems*, 11.
- 314 Herrington, A. R., & Reed, K. A. (2020). On resolution sensitivity in the commu-  
315 nity atmosphere model. *Quarterly Journal of the Royal Meteorological Society*,  
316 146(733), 3789–3807.
- 317 Hurrell, J. W., Hack, J. J., Shea, D., Caron, J. M., & Rosinski, J. (2008). A new  
318 sea surface temperature and sea ice boundary dataset for the community at-  
319 mosphere model. *Journal of Climate*, 21(19), 5145–5153.
- 320 Jablonowski, C., & Williamson, D. L. (2006). A baroclinic instability test case for  
321 atmospheric model dynamical cores. *Q. J. R. Meteorol. Soc.*, 132, 2943–2975.
- 322 Jablonowski, C., & Williamson, D. L. (2011). The pros and cons of diffusion, fil-  
323 ters and fixers in atmospheric general circulation models., in: P.H. Lauritzen,  
324 R.D. Nair, C. Jablonowski, M. Taylor (Eds.), Numerical techniques for global  
325 atmospheric models. *Lecture Notes in Computational Science and Engineering*,  
326 Springer, 80.
- 327 Lauritzen, P. H., Bacmeister, J. T., Callaghan, P. F., & Taylor, M. A. (2015). Near  
328 global model topography generation software for unstructured grids. *Geosci-  
329 entific Model Development Discussions*, 8(6), 4623–4651. doi: 10.5194/gmdd-8  
330 –4623-2015
- 331 Lauritzen, P. H., Mirin, A., Truesdale, J., Raeder, K., Anderson, J., Bacmeister, J.,  
332 & Neale, R. B. (2011). Implementation of new diffusion/filtering operators  
333 in the CAM-FV dynamical core. *Int. J. High Perform. Comput. Appl.*. doi:

**Figure 6.** .

334

10.1177/1094342011410088

335

Lauritzen, P. H., Nair, R., Herrington, A., Callaghan, P., Goldhaber, S., Dennis, J., ... Dubos, T. (2018). NCAR CESM2.0 release of CAM-SE: A reformulation of the spectral-element dynamical core in dry-mass vertical coordinates with comprehensive treatment of condensates and energy. *J. Adv. Model. Earth Syst.*. doi: 10.1029/2017MS001257

340

Lauritzen, P. H., Taylor, M. A., Overfelt, J., Ullrich, P. A., Nair, R. D., Goldhaber, S., & Kelly, R. (2017). CAM-SE-CSLAM: Consistent coupling of a conservative semi-lagrangian finite-volume method with spectral element dynamics. *Mon. Wea. Rev.*, 145(3), 833-855. doi: 10.1175/MWR-D-16-0258.1

344

Lin, S.-J. (2004). A 'vertically Lagrangian' finite-volume dynamical core for global models. *Mon. Wea. Rev.*, 132, 2293-2307.

346

Lin, S.-J., & Rood, R. B. (1997). An explicit flux-form semi-Lagrangian shallow-water model on the sphere. *Q.J.R.Meteorol.Soc.*, 123, 2477-2498.

348

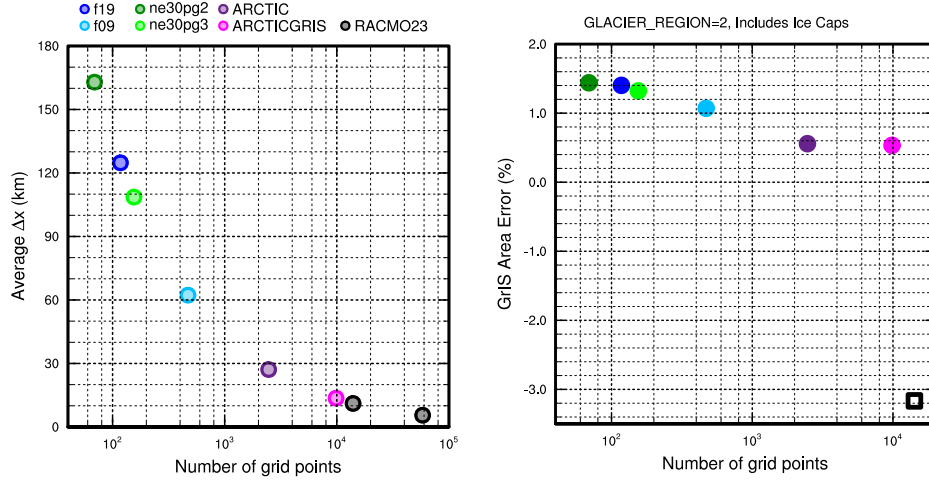
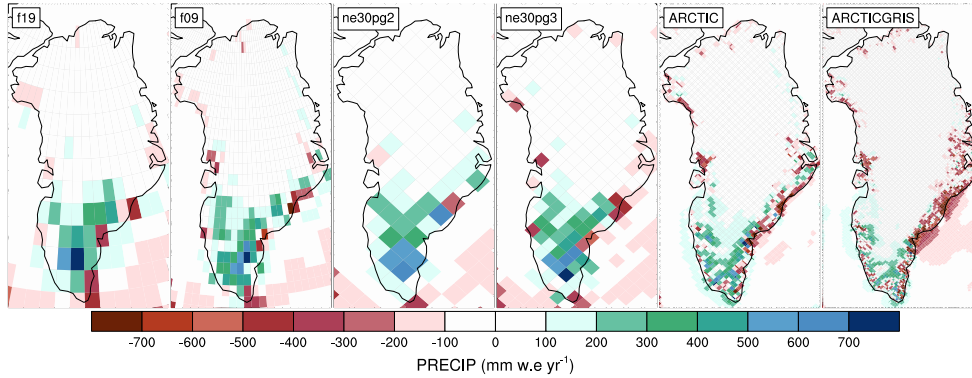
Lofverstrom, M., Fyke, J. G., Thayer-Calder, K., Muntjewerf, L., Vizcaino, M., Sacks, W. J., ... Bradley, S. L. (2020). An efficient ice sheet/earth system model spin-up procedure for cesm2-cism2: Description, evaluation, and broader applicability. *Journal of Advances in Modeling Earth Systems*, 12(8), e2019MS001984.

353

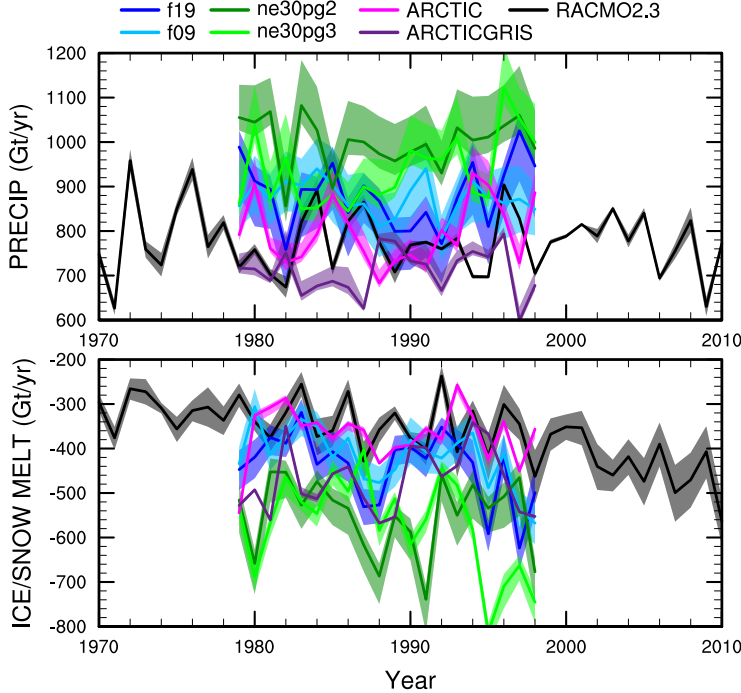
Neale, R. B., Richter, J. H., & Jochum, M. (2008). The impact of convection on ENSO: From a delayed oscillator to a series of events. *J. Climate*, 21, 5904-5924.

355

Noël, B., van de Berg, W. J., Lhermitte, S., & van den Broeke, M. R. (2019). Rapid

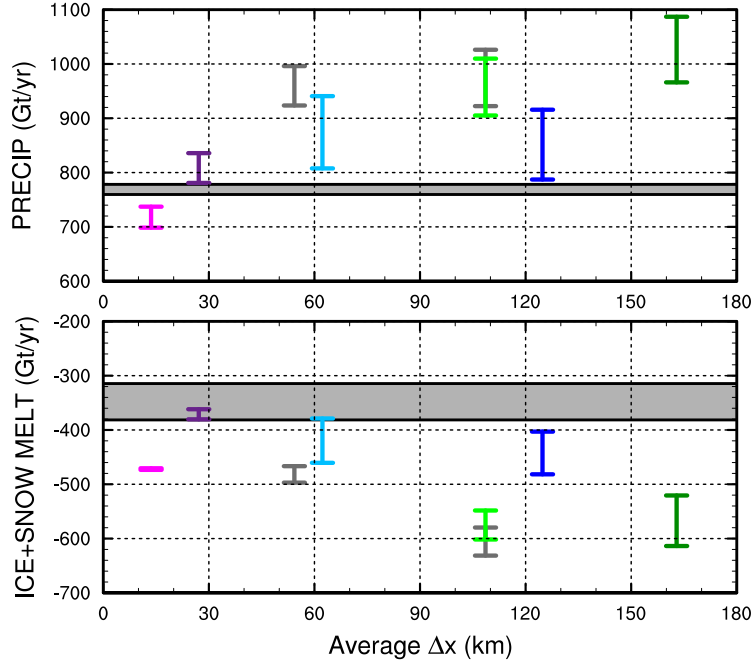
**Figure 7.** .**Figure 8.** Climatological (1979–1998) annual precipitation rate bias relative to the RACMO2.3p2 5.5km resolution data product (Noël et al., 2019).

- ablation zone expansion amplifies north greenland mass loss. *Science advances*, 5(9), eaaw0123.
- O'Brien, T. A., Collins, W. D., Kashinath, K., Rübel, O., Byna, S., Gu, J., ... Ullrich, P. A. (2016). Resolution dependence of precipitation statistical fidelity in hindcast simulations. *J. Adv. Model. Earth Syst.*, 8(2), 976–990. Retrieved from <http://dx.doi.org/10.1002/2016ms000671> doi: 10.1002/2016ms000671
- Pope, V., & Stratton, R. (2002). The processes governing horizontal resolution sensitivity in a climate model. *Climate Dynamics*, 19(3–4), 211–236.
- Putman, W. M., & Lin, S.-J. (2007). Finite-volume transport on various cubed-sphere grids. *J. Comput. Phys.*, 227(1), 55–78.
- Richter, J. H., Sassi, F., & Garcia, R. R. (2010). Toward a physically based gravity wave source parameterization in a general circulation model. *J. Atmos. Sci.*, 67, 136–156. doi: dx.doi.org/10.1175/2009JAS3112.1
- Roeckner, E., Brokopf, R., Esch, M., Giorgetta, M., Hagemann, S., Kornblueh, L., ... Schulzweida, U. (2006). Sensitivity of simulated climate to horizontal and vertical resolution in the echam5 atmosphere model. *Journal of Climate*, 19(16), 3771–3791.



**Figure 9.** Time-series of annual (solid+liquid) precipitation (top) and annual runoff (bottom) integrated over the Greenland Ice Sheet for all six simulations and compared to RACMO3.2. The raw fields are mapped to two target low resolution grids, f19 & ne30pg2, and using two different remapping methods, conservative ESMF and high order TempestRemap. The remapped values are then integrated over the ice mask of the target grid. This gives four time-series for each simulation (three for f19 & ne30pg2), with the mean value given by the solid line and shading spanning the extent of the remapped solutions.

- 375 Smirnova, J., & Golubkin, P. (2017). Comparing polar lows in atmospheric reanalyses: Arctic system reanalysis versus era-interim. *Monthly Weather Review*,  
376 145(6), 2375–2383.  
377  
378 Stocker, T. (2014). *Climate change 2013: the physical science basis: Working group i contribution to the fifth assessment report of the intergovernmental panel on climate change*. Cambridge university press.  
379  
380 Suarez, M. J., & Takacs, L. L. (1995). Volume 5 documentation of the aries/geos dynamical core: Version 2.  
381  
382 Taylor, M. A., Tribbia, J., & Iskandarani, M. (1997). The spectral element method  
383 for the shallow water equations on the sphere. *J. Comput. Phys.*, 130, 92-108.  
384 Ullrich, P. A., Zarzycki, C. M., McClenney, E. E., Pinheiro, M. C., Stansfield, A. M.,  
385 & Reed, K. A. (2021). Tempestextremes v2. 1: a community framework for  
386 feature detection, tracking and analysis in large datasets. *Geoscientific Model  
387 Development Discussions*, 1–37.  
388  
389 van Kampenhout, L., Lenaerts, J. T., Lipscomb, W. H., Lhermitte, S., Noël, B.,  
390 Vizcaíno, M., ... van den Broeke, M. R. (2020). Present-day greenland ice  
391 sheet climate and surface mass balance in cesm2. *Journal of Geophysical  
392 Research: Earth Surface*, 125(2), e2019JF005318.  
393  
394 van Kampenhout, L., Rhoades, A. M., Herrington, A. R., Zarzycki, C. M., Lenaerts,  
J. T. M., Sacks, W. J., & van den Broeke, M. R. (2018). Regional grid refine-

**Figure 10.** .

- 395      ment in an earth system model: Impacts on the simulated greenland surface  
 396      mass balance. *The Cryosphere Discuss..* doi: 10.5194/tc-2018-257  
 397      Williamson, D. (2007). The evolution of dynamical cores for global atmospheric  
 398      models. *J. Meteor. Soc. Japan*, 85, 241-269.  
 399      Williamson, D. L. (2008). Convergence of aqua-planet simulations with increas-  
 400      ing resolution in the community atmospheric model, version 3. *Tellus A*, 60(5),  
 401      848–862. doi: 10.1111/j.1600-0870.2008.00339.x  
 402      Zhang, G., & McFarlane, N. (1995). Sensitivity of climate simulations to the pa-  
 403      rameterization of cumulus convection in the canadian climate centre general  
 404      circulation model. *Atmosphere-ocean*, 33(3), 407-446.

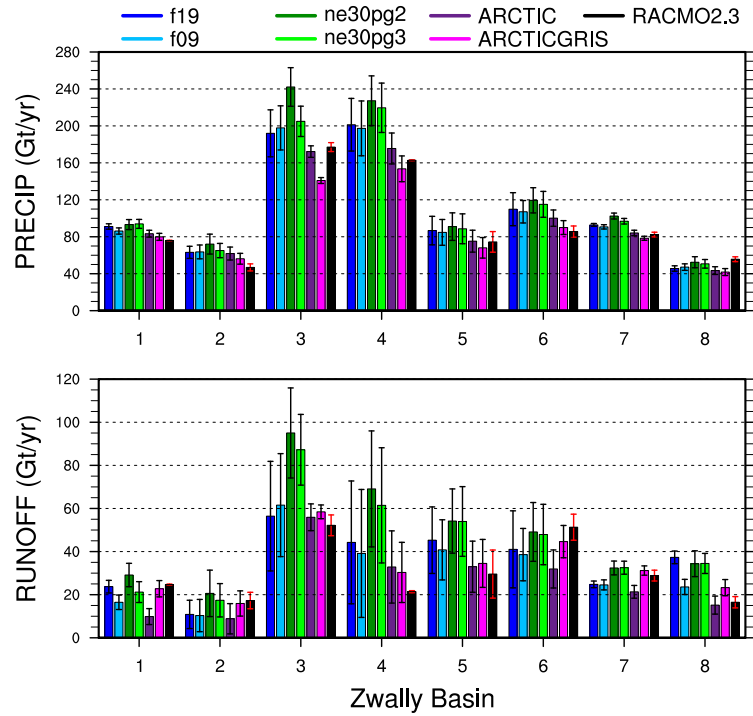


Figure 11. .

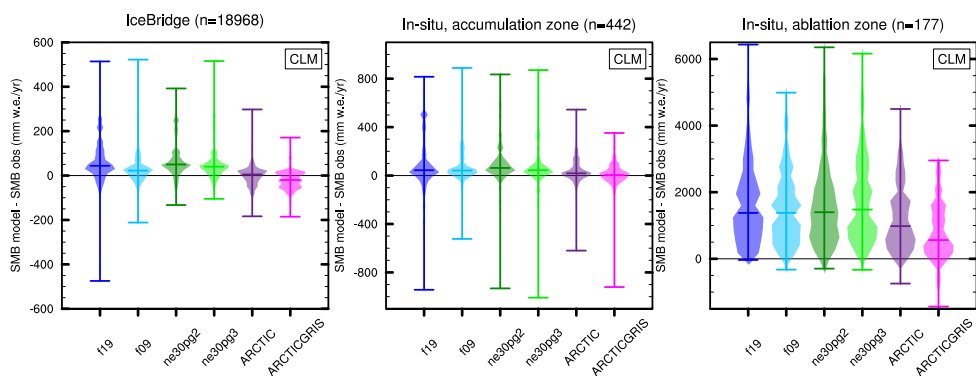
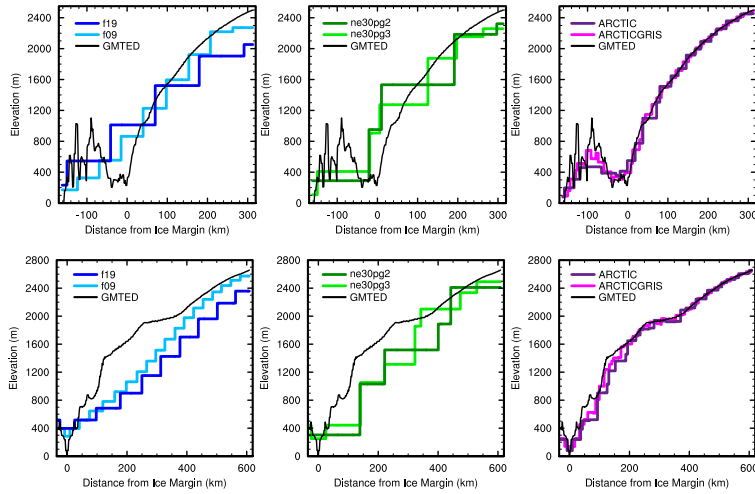
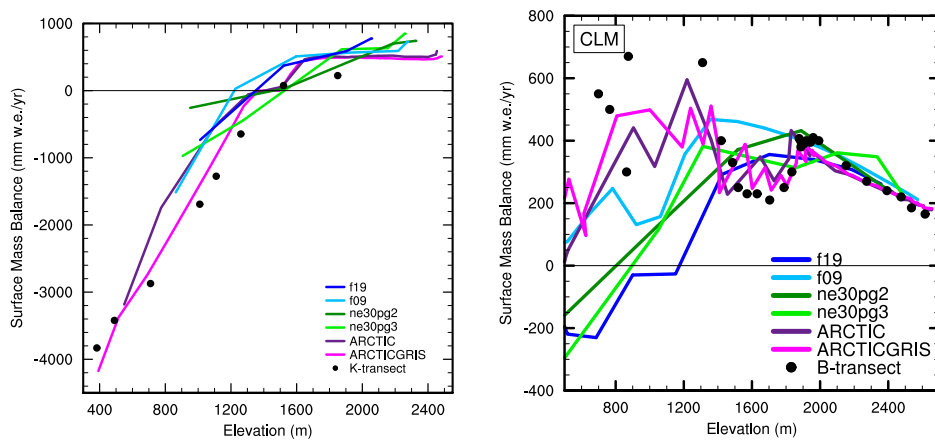


Figure 12. .



**Figure 13.** .



**Figure 14.** .